Pergamon

Int. J. Heat Mass Transfer. Vol. 37, No. 17, pp. 2647–2660, 1994

0017–9310/94 $7.00 + 0.00

0017–9310(94)E0103–2

Theoretical and physical interpretation of entrainment phenomenon in capillary-driven heat pipes using hydrodynamic instability theories

B. H. KIM and G. P. PETERSON†

Department of Mechanical Engineering, Texas A&M University, College Station, TX 77843-3123, U.S.A.

(*Received* 4 *August* 1993 *and in final form* 18 *March* 1994)

Abstract—The entrainment phenomenon in two-phase parallel flow has been studied from the standpoint of wave instability theories, which are related to the exponential growth of unstable waves caused by viscous interaction between the two parallel flowing fluids. Instability theories related to the Kelvin–Helmholtz and the Orr–Sommerfeld problems were reviewed and applied to predict the critical air/vapor velocity at the onset of entrainment from a capillary structure. To compare the theoretical criteria with the experimental results, entrainment observed in both air–water and steam–water situations were characterized and classified into three major categories. As results of these comparisons, a modified theoretical criterion based on the results of Miles was developed and used to investigate the effect of liquid depth on the critical air/vapor velocity or corresponding Weber number for the given temperatures, and general trends of the various criteria were examined as a function of vapor temperature.

INTRODUCTION

IN MOST operating thermosyphons and heat pipes, the liquid flows in the opposite direction to the vapor flow. At high thermal powers, the viscous shear forces occurring at the liquid/vapor interface may inhibit the return of liquid to the evaporator. As a result of the interaction between the counterflowing liquid and vapor, the liquid flow on the interface becomes stagnant or concurrent with the high velocity vapor flow. Subsequently, capillary waves arise on the liquid surface, and their amplitude may grow with increases in vapor velocity.

With further increases in the vapor velocity, the interfacial shear force may become sufficient to overcome the liquid surface-tension force and to cause liquid droplets to be stripped or torn off the wavy liquid/vapor interface and entrained into the vapor flow [1]. This entrainment of liquid droplets leads to the partial or total stoppage of liquid flow or dry-out and limits the axial heat transport, which is referred to as the entrainment limit [2, 3].

To predict the critical air/vapor velocity at the onset of entrainment from the wicked interface, Cotter [4] first introduced the instability concept for operating heat pipes, but this approach has not been well recognized. The entrainment phenomenon in two-phase parallel flow has been studied from the standpoint of wave instability theories, which are related to the exponential growth of unstable waves caused by viscous interaction between the two parallel flowing fluids. In reality, the physical mechanisms for entrainment and unstable wave generation are slightly different, but the wave instability theories can be regarded as a lower bound for the prediction of entrainment onset air/vapor velocity since entrainment is a subsequent phenomenon to the onset of unstable waves.

The problem of wave instability was first investigated by Lord Kelvin [5], who was motivated to predict the critical wind speed corresponding to the generation of unstable water waves. It is sometimes called inviscid Kelvin–Helmholtz (K–H) instability since it is restricted to two-dimensional motion of two inviscid parallel fluids with infinite vertical extent. Hence, it does not agree with actual flow situations associated with a wavy interface subjected to turbulent shear flow. Thus, the theoretically predicted critical air/vapor velocity for the onset of unstable waves is significantly higher than the corresponding experimental observations [6–9].

In 1925, Jeffreys introduced the 'sheltering hypothesis' to explain the disagreement between K–H analysis and experimental results and developed a viscous K–H instability including a viscous term for the lighter fluid, which shows good agreement with experimental observations.

In addition, Lamb [10] investigated the effects of depth (in feet) as well as viscosity on the maintenance of waves, and claimed that the possibility of pro-

†Author to whom correspondence should be addressed.

NOMENCLATURE

a constant
A_v vapor cross-sectional area [m^2]
c wave phase speed [m s^{-1}]
C_s sheltering coefficient
c_p specific heat of the coolant [kJ kg^{-1} K^{-1}]
d_1 wire spacing [m]
d_2 thickness of the wick [m]
D differential operator, $\partial/\partial z$
dn element of the outward normal
dS surface area of the liquid element [m^2]
dV volume of the liquid element [m^3]
E disturbance function
F equation of eigenvalues
Fr Froude number
h liquid film thickness [m]
l direction cosine in x direction
m direction cosine in y direction
$\dot{m}$ coolant mass flow rate [kg s^{-1}]
n direction cosine in z direction
N_{vi} viscosity number or Taylor number
P_i pressure of the ith component of fluids [Pa]
$\hat{P}$ basic solution of pressure distribution [Pa]
$\bar{P}_i$ pressure of the ith component of fluids in the basic flow [Pa]
P_i' fluctuation of pressure in the ith component of fluid [Pa]
P_0 dimensionless static pressure
q_{ec} entrainment limit [W]
r radius of curvature on the interface in equations (6) and (7) [m]
r differential operator, Laplacian ∇^2 in equations (16) and (17)
Re Reynolds number
s growth rate of waves
T temperature of fluids (K)
$\mathbf{u}_i$ velocity vector of the ith component of fluids [m s^{-1}]
$\mathbf{u}_i'$ perturbation velocity vector of the ith component of fluids [m s^{-1}]
$\mathbf{U}_i$ vector of the ith component of fluids in the basic flow [m s^{-1}]
U_{vc} critical air/vapor velocity [m s^{-1}]
$\hat{u}_i$ velocity function in equation (8) for the ith component of fluids in x direction [m s^{-1}]
U_l liquid surface velocity [m s^{-1}]
v velocity component in y direction [m s^{-1}]
w velocity component in z direction [m s^{-1}]
$\hat{w}_i$ velocity function in equation (8) for the ith component of fluids in z direction [m s^{-1}]
We Weber number.

Greek symbols

α wave number in the x direction [m^{-1}]
$\tilde{\alpha}$ harmonic mean of α and β [m^{-1}]
β wave number in the y direction [m^{-1}]
ζ arbitrary disturbance in the z direction [m]
η zx component of rotation tensor [s^{-1}]
λ wave length [m]
λ_c critical wave length [m]
μ viscosity of fluids [Pa s]
ν kinematic viscosity of fluids [m^2 s^{-1}]
ξ yz component of rotation tensor [s^{-1}]
ϕ velocity potential of the liquid flow
Φ total viscous dissipation rate [J s^{-1}]
ψ' fluctuation in the liquid stream function.

Subscripts

c critical values at the onset of instability or entrainment
i ith component of fluids
l liquid
v vapor
t derivative with respect to time.

gressive waves is limited to the case of a uniform depth that exceeds half of the wave length. Lamb's work was extended by Jeffreys [11] and Bondi [12] to cover the case when the liquid is comparatively shallow (in centimeters).

The stability problem for a thin film of liquid having a linear velocity profile and bounded by a fixed wall and a free surface was first investigated by Feldman [13], who solved two Orr–Sommerfeld equations for both liquid film and vapor flow having linear profiles. However, results of the theoretical prediction showed that the minimum value of the critical Reynolds number corresponding to instability of the liquid film was significantly larger than that observed in experiments. This problem was modified by Miles [14] and solved asymptotically for large values of film Reynolds number in accordance with Heisenberg's criterion that neutral disturbances having a finite wave number and phase velocity for $Re_l = \infty$ are necessarily unstable as $Re_l \to \infty$.

The major objectives of the present study are first to review important assumptions, basic equations and boundary conditions incorporated in the derivation of theoretical criteria and second, to compare the theoretical results with those from both air–water and steam–water experiments.

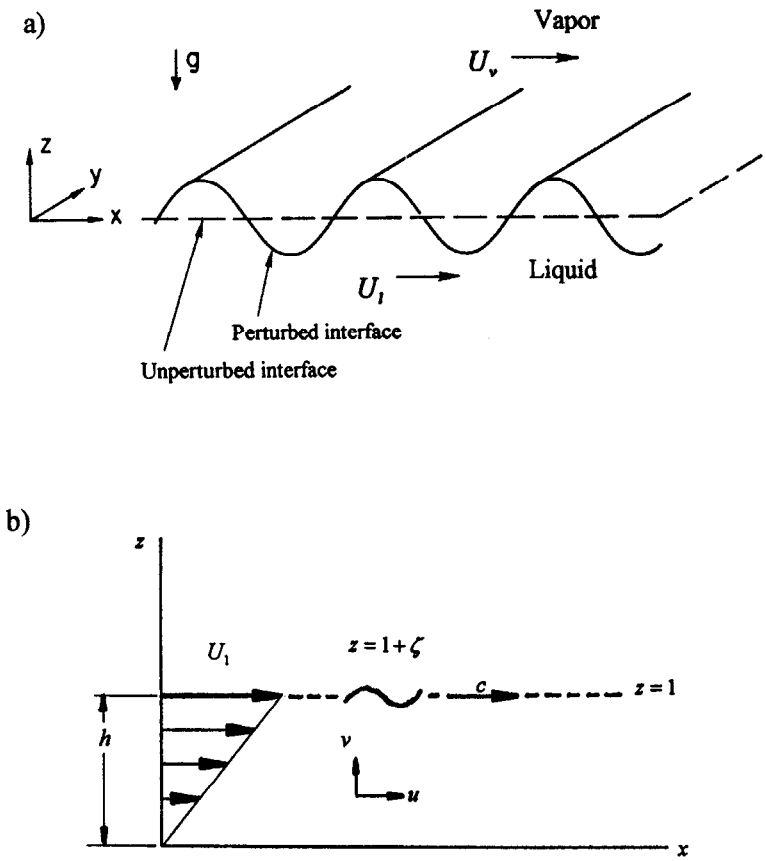

FIG. 1. Configuration of perturbed interface in linear analysis of (a) inviscid K–H instability [26], (b) viscous O–S instability [14].

BACKGROUND AND PREVIOUS STUDIES

For convenience, wave instability theories of interest here can be classified into two types, Kelvin–Helmholtz (K–H) and Orr–Sommerfeld (O–S). These two types are both closely related to the entrainment modes observed in air–water and steam–water experiments.

K–H type instability

The ideal case of inviscid K–H type instability will be discussed first. Initially, the interface between the two phases can be assumed to be a flat horizontal plane at $z = 0$, as illustrated in Fig. 1(a). The liquid and vapor phases are moving in the x direction with free-stream velocities U_l and U_v with respect to the undisturbed interface. The analysis is restricted to two-dimensional arbitrary disturbances $\zeta(x, t)$ and to incompressible and inviscid fluids with infinite vertical extents. With these assumptions, the basic equations for the subsequent fluid motion in the two fluids ($i = 1, 2$, for liquid and vapor, respectively) are two-dimensional forms of the Navier–Stokes equations, from which a perturbation equation can be derived by letting

$$\mathbf{u}_i = \mathbf{U}_i + \mathbf{u}_i' \quad P_i = \bar{P}_i + P_i' \tag{1}$$

$$\nabla \cdot \mathbf{u}_i' = 0 \tag{2}$$

$$\mathbf{u}_{it}' + \mathbf{U}_i \cdot \nabla \mathbf{u}_i' = -\frac{1}{\rho} \nabla P_i'. \tag{3}$$

From equation (2) and (3), we can obtain

$$\Delta P_i' = 0. \tag{4}$$

P_i' $(i = 1)$ and $\mathbf{u}_i'$ $(i = 1, 2)$ vanish as z goes to $\pm\infty$ and

$$w_i' = \frac{\mathrm{D}\zeta}{\mathrm{D}t} \quad at \quad z = 0. \tag{5}$$

In addition, the force balance normal to the interface becomes the Young–Laplace equation since the perturbation velocity normal to the interface is usually small, and hence the contribution to the corresponding force momentum equation is negligible.

$$P_l - P_v = \sigma\left(\frac{1}{r_1} + \frac{1}{r_2}\right). \tag{6}$$

From the geometry of the interface,

$$\frac{1}{r_1} = \frac{(\partial^2\zeta/\partial x^2)}{[1 + (\partial\zeta/\partial x)^2]^{3/2}} \quad \frac{1}{r_2} = 0. \tag{7}$$

Following the usual procedure of linear stability

analysis, perturbation quantities such as velocities and pressures are determined by defining them as

$$\mathbf{u}_i' = (\hat{u}_i(z), \hat{w}_i(z))\, e^{i\alpha x + st} \quad P' = \hat{P}(z) e^{i\alpha x + st}$$
$$\zeta = A e^{i\alpha x + st}. \tag{8}$$

Substituting equation (8) into equations (4) and (5) and using the given boundary conditions, an eigenvalue relation for s in terms of α can be obtained by eliminating A.

$$s = \pm \frac{\{\alpha^2 \rho_l \rho_v (U_l - U_v)^2 - [\sigma\alpha^3 + (\rho_l - \rho_v) g\alpha](\rho_l + \rho_v)\}^{1/2}}{\rho_l + \rho_v} - \frac{i\alpha(\rho_l U_l + \rho_v U_v)}{\rho_l + \rho_v}. \tag{9}$$

For this case, s should have a non-zero real term to satisfy the condition for an unstable interface whose amplitude for the perturbation will grow with time, i.e.

$$|U_l - U_v| > \left(\frac{[\sigma\alpha + (\rho_l - \rho_v) g/\alpha](\rho_l + \rho_v)}{\rho_l \rho_v}\right)^{1/2}. \tag{10}$$

The right side of this inequality has a minimum value at a critical wave number that is equal to

$$\alpha_c = \left(\frac{(\rho_l - \rho_v) g}{\sigma}\right)^{1/2}. \tag{11}$$

As a result, the interface will be unstable when $|U_l - U_v|$ is greater than U_{vc} derived from the right side of equation (4) using the value α_c given in equation (5).

$$U_{vc} = \left(\frac{2(\rho_l + \rho_v)}{\rho_l}\right)^{1/2} \left(\frac{\sigma(\rho_l - \rho_v) g}{\rho_v^2}\right)^{1/4}. \tag{12}$$

The critical wave length corresponding to the critical wave number is obtained from the relation, $\lambda_c = 2\pi/\alpha_c$. By assuming $g = 0$ and $\rho_l \gg \rho_v$ in equation (10), Cotter [4] presented a different critical air/vapor velocity using equation (13) for the case of very short waves, whose wave length was nearly equal to the wire spacings of the capillary-wick, i.e.

$$\lambda_c = 2\pi \left(\frac{\sigma}{(\rho_l - \rho_v)}\right)^{1/2} \tag{13}$$

$$U_{vc} = \left(\frac{2\pi\sigma}{\rho_v \lambda_c}\right)^{1/2}. \tag{14}$$

Equation (14) was experimentally verified using an air–water test channel by Matveev *et al.* [15] and Kim *et al.* [16].

As noted earlier, the theoretical critical air/vapor velocity obtained from equation (12) is significantly larger than those observed in experimental investigations. To better predict the critical air/vapor velocity, Jeffreys [7] developed a modified K–H instability theory by introducing the 'sheltering hypothesis', which explains the effect of the velocity discontinuity due to vortices induced by boundary-layer separation in the leeward direction of the liquid waves [6, 8]. The regions sheltered from the main vapor stream are contained within swirling eddies, which cause enhanced vertical momentum and mass transfer.

For viscous motion of the liquid flow, a viscous dissipation term is included in the momentum perturbation equation given in equation (3).

$$\mathbf{u}_t' + \mathbf{U} \cdot \nabla \mathbf{u}' = -\frac{1}{\rho_l} \nabla P' + \nu_l \Delta u'. \tag{15}$$

Using the same procedure used for the inviscid K–H analysis and assuming no tangential reaction on the interface, a complementary equation in terms of ζ can be obtained from the normal pressure balance at $z = 0$ as

$$\left[\left(\frac{\partial}{\partial t} + U_l \frac{\partial}{\partial x} + 2\nu_l r^2\right)^2 + c^2 r^2 - C_s \frac{\rho_v}{\rho_l} U_v^2 \left(\frac{\partial}{\partial x} r\right)\right] \zeta = 0 \tag{16}$$

where r is a differential operator,

$$\frac{\partial^2}{\partial x^2} + \frac{\partial^2}{\partial y^2}$$

and

$$\rho_l c^2 = \frac{g}{r}(\rho_l - \rho_v) + \sigma r. \tag{17}$$

The last term in equation (16) was introduced according to the sheltering hypothesis and represents the pressure exerted by air/vapor flow on the ascending side of the wave. If $\zeta \propto e^{i(\alpha x + \beta y) + st}$, then equation (16) becomes

$$[(s + 2\nu_l \tilde{\alpha}^2)^2 + c^2 \tilde{\alpha}^2 - U_l^2 \alpha^2]\zeta + \left(2U_l(s + 2\nu_l \tilde{\alpha}^2) - \frac{C_s \rho_v}{\rho_l} U_v^2 \tilde{\alpha}\right) \frac{\partial \zeta}{\partial x} = 0 \tag{18}$$

where $\tilde{\alpha} = (\alpha^2 + \beta^2)^{1/2}$. By neglecting the terms, $(s + \nu_l \tilde{\alpha}^2)^2$ and $\nu_l \tilde{\alpha}^2$, Jeffreys [7] obtained an eigenvalue relation, $F(s, \alpha, \beta) = 0$, by letting both coefficients for ζ and $\partial\zeta/\partial x$ be zero. If the surface tension term in the right-hand side of equation (17) is neglected for small wave numbers, the unstable condition for the positive s leads to an instability criterion in terms of the relative air/vapor velocity, U_r, to the liquid as

$$U_r^3 \geqslant \frac{27 \nu_l g}{C_s} \frac{\rho_l - \rho_v}{\rho_l}. \tag{19}$$

As indicated in equation (17), the surface tension term is no longer negligible for the case of increased wave number, which is observed in the finite depth of water subjected to air/vapor blowing.

Jeffreys [11] extended the viscous theory applied to the two infinite fluids to the case of uniform and finite

depth h. For irrotational liquid flow, a velocity potential is obtained from Laplace's equation.

$$(D^2-r^2)\phi = 0 \tag{20}$$

$$\phi = U_l x + Ae^{rz} + Be^{rz}. \tag{21}$$

Constants A and B are determined in terms of ζ by a kinematic condition at the surface $z = 0$ and no slip boundary condition at the bottom $z = -h$, i.e.

$$w = \frac{\partial\phi}{\partial z} = r(A-B) = \frac{D\zeta}{Dt} \tag{22}$$

$$e^{-rh}A - e^{rh}B = 0. \tag{23}$$

From these equations, the velocity potential in equation (21) can be obtained as

$$\phi = \frac{sa}{\tilde{\alpha}}\frac{\cosh\tilde{\alpha}(z+h)}{\sinh(\tilde{\alpha}h)}\sin(st-\alpha x)\cos(\beta y). \tag{24}$$

Using this velocity potential for liquid flow, a complete calculation of the total viscous dissipation rate, Φ, was presented by Bondi [12] according to the formula given in Lamb [10].

$$\Phi = 4\mu_l\iiint(\xi^2+\eta^2+\varsigma^2)\,dV + \mu_l\iint\frac{\partial|\mathbf{u}|^2}{\partial n}dS - 4\mu_l\iint\begin{vmatrix} l & m & n \\ u & v & w \\ \xi & \eta & \varsigma \end{vmatrix}dS \tag{25}$$

where l, m and n are direction cosines of the normal to the surface and ξ, η and ς are rotation vectors. The contribution of the last integral is negligible since $u = v = w = 0$ at the bottom and vorticity is small on the liquid surface. The second integral was calculated by Jeffreys [11] as $\mu_l\tilde{\alpha}s^2a^2\coth\tilde{\alpha}h$ and the first integral was obtained by Bondi [12] as $\rho_l s^2a^2\sqrt{(0.5sv_l)}/(4\sinh^2\tilde{\alpha}h)$.

In addition, the mean value of the pressure work by the air/vapor was determined by Jeffreys [11] as $C_s\rho_v(U_v-c)^2s\alpha a^2/4$, where U_v-c is the velocity of the air/vapor flow relative to the crests and C_s is the sheltering coefficient. Hence the wave will grow if the pressure work done on the liquid is larger than the energy dissipated given in equation (25). The criterion for surface instability was proposed by Bondi [12] as

$$\frac{1}{4}C_s\rho_v(U_v-c)^2s\alpha a^2 \geqslant \mu_l\tilde{\alpha}s^2a^2\coth\tilde{\alpha}h + \frac{\rho_l s^2a^2}{4\sinh^2\tilde{\alpha}h}\sqrt{(0.5sv_l)} \tag{26}$$

where c is obtained from equation (18), as

$$\alpha^2c^2 = s^2 = \left(g\frac{\rho_l-\rho_v}{\rho_l} + \frac{\sigma}{\rho_l}\tilde{\alpha}^2\right)\tilde{\alpha}\tanh\tilde{\alpha}h. \tag{27}$$

If $\tilde{\alpha}$ is maintained constant, then equation (26) is more likely to be satisfied as c decreases or α increases. The most unstable waves are two-dimensional and their wave number, α, approaches $\tilde{\alpha}$ according to Squire's theorem [17]. Thus equations (26) and (27) become

$$U_v = c + \left\{\frac{4\rho_l c}{C_s\rho_v}\left[\frac{v_l\alpha}{\tanh\alpha h} + \sqrt{\left(\frac{v_l\alpha c}{2}\right)\frac{1}{4\sinh^2\alpha h}}\right]\right\}^{1/2} \tag{28}$$

$$c^2 = \left(\frac{1}{\alpha}g\frac{\rho_l-\rho_v}{\rho_l} + \frac{\sigma}{\rho_l}\alpha\right)\tanh\alpha h. \tag{29}$$

O–S type instability

An approximate determination of the instability criterion for thin film flow was investigated for larger values of Reynolds numbers in accordance with Heisenberg's criterion that neutral disturbances having a finite wave number and phase velocity for $Re_l = \infty$ are necessarily unstable as $Re_l \to \infty$ [14]. The thin film of liquid flow is assumed to be incompressible, two-dimensional and laminar, and to be bounded below by a wall and subjected to a parallel flow of less dense fluid. Also, Miles [14] claimed, based upon experimental data [18], that the most significant role of the lighter fluid is to produce the mean shear flow illustrated in Fig. 1(b) provided the density ratio to the heavier liquid is very small and the kinematic viscosity ratio is large. As a result, turbulent fluctuations in the lighter fluid may not significantly change the wave formation at the interface.

If the governing equations, equations (2) and (15), are non-dimensionalized using reference quantities, h, U_l and $\rho_l U_l^2$, the equilibrium flow shown in Fig. 1(b) can be specified by dimensionless variables as

$$U(z) = z \quad P = P_0 \quad \tau = \tau_0 = Re_l^{-1} \tag{30}$$

where P_0 is dimensionless static pressure. This equilibrium flow is superimposed onto small disturbances expressed as

$$E(x,t) = e^{i\alpha(x-ct)}. \tag{31}$$

The perturbation velocity components in equation (15) are defined by a perturbation stream function as

$$\psi'(x,z,t) = \phi(z)E(x,t) \tag{32}$$

$$u' = -\psi'_z = -(D\phi)E \quad v' = \psi'_x = i\alpha\phi E \tag{33a, b}.$$

Also, the displacement of any stream line (in particular the free interface or interface at $z \approx 1$) is given by

$$\psi = (U_l - c)\zeta. \tag{34}$$

Substituting equation (33a, b) into the governing equations (2) and (15), the Orr–Sommerfeld equation and perturbation pressure and shear stress can be obtained from Lin [19] as

$$(U-c)(D^2\phi-\alpha^2\phi) = (i\alpha Re_l)^{-1}(D^4\phi - 2\alpha^2D^2\phi + \alpha^4\phi) \tag{35}$$

$$P' = \left[(U_l - c)D\phi - \frac{\partial U_l}{\partial z}\phi - (i\alpha Re_l)^{-1}(D^3\phi - \alpha^2 D^2\phi) \right] E \quad (36)$$

$$\tau = Re_l^{-1}(u_z' + v_x') = -Re_l^{-1}(D^2\phi + \alpha^2\phi)E. \quad (37)$$

There are four boundary conditions. Two of them are no-slip conditions at $z = 0$ and the others are the result of a normal pressure balance and a no-shear-stress condition at the interface, $z = 1$.

$$u' = v' = 0 \quad \text{at } z = 0 \quad (38a, b)$$

$$-P' + 2Re_l^{-1}v_z' = (1/We_l)\zeta_{xy} - (1/Fr)\zeta \quad \tau = 0 \quad \text{at } z = 1 \quad (38c, d)$$

where We_l and Fr represent the Weber and Froud number for the liquid. Substituting equation (33a, b), (34), (36) and (37) into equation (38a, b, c, d), yields

$$\phi = D\phi = 0 \quad \text{at } z = 0 \quad (39a, b)$$

$$\bar{\omega} = (1-c)D\phi - \phi - (i\alpha Re_l)^{-1}(D^3\phi - 3\alpha^2 D\phi) - \left(\frac{\alpha^2}{We_l} + \frac{1}{Fr}\right)(1-c)^{-1}\phi = 0 \quad \text{at } z = 1 \quad (39c)$$

$$D^2\phi + \alpha^2\phi = 0 \quad \text{at } z = 1. \quad (39d)$$

Four linearly independent solutions to equation (35) were obtained by Feldman [13]. Substituting the asymptotic solution proposed by Lin [20] into equations (39a)–(39d), an eigenvalue relation can be obtained. In the case of $Re_l = \infty$, the relation leads to

$$\alpha \coth \alpha (1-c)^2 - (1-c) - \left(\frac{\alpha^2}{We_l} + \frac{1}{Fr}\right) = 0. \quad (40)$$

The roots, c_0, of equation (40) are obtained as

$$c_0 = 1 - \left(\frac{1 \pm \{1 + 4[(\alpha^2/We_l) + (1/Fr)]\alpha \coth \alpha\}}{2\alpha \coth \alpha} \right). \quad (41)$$

The flow is stable if $0 < c_0 < 1$, which implies there can be no energy transfer between an inviscid shear flow and a traveling wave disturbance [23]. These roots correspond to the positive radical in (0, 1) if and only if

$$f(\alpha) = \alpha \coth \alpha - 1 - \frac{\alpha^2}{We_l} - \frac{1}{Fr} > 0. \quad (42)$$

By examining $f(\alpha)$, Miles [14] found that $We_l < 3$ is a sufficient condition for stability as Re_l goes to infinity.

DESCRIPTION OF EXPERIMENT

Two different experiments have been conducted; air–water [16] and the present steam–water experiment using the heat pipe in Fig. 2. For the air–water experiment, the critical air velocity at the onset of entrainment was measured by a laser diffraction particle sizer, which is devised to detect water droplets in the air stream. Because it is very difficult to directly measure corresponding vapor velocity in the steam–water experiment, the critical vapor velocity was indirectly calculated using an energy balance equation [21],

$$U_{vc} = \frac{q_{ec}}{\rho_v A_v h_{fg}} \quad (43)$$

where q_{ec} is the heat transfer rate (W) at the onset of entrainment, and A_v and h_{fg} are the vapor cross-sectional area (m^2) and latent heat of vaporization (J kg^{-1}), respectively. The uncertainty in the estimation of the critical velocity may be regarded as that involved in entrainment limit measurements, which will be discussed in equation (44). In the present steam–water experiments, the heat pipe was placed on a horizontal plane and entrainment limit measurements were performed without tilting.

Steam–water experiment

The heat pipe used in the current investigation was constructed from copper tubes and a rectangular copper duct as shown in Fig. 2. The entire length of the heat pipe was approximately 2.16 m, long enough to apply a maximum power of 7.24 kW prior to dry-out. Both the evaporator and condenser were made of 0.76 m long copper tubes with an inner diameter of 76 mm. The adiabatic section was fabricated from a 0.64 m long rectangular copper duct. The vapor flow section of the adiabatic region is 25 mm wide and 15.7 mm high, and the liquid flow section is 25 mm wide and 12.7 mm high.

In the adiabatic region (test section), six viewing windows were installed for flow visualization of the wicked interface. The copper mesh (mesh number 40) to be evaluated was inserted into an axially-machined slit, under which 10 layers of copper mesh (mesh number 24) were installed to supply water to the evaporator. To minimize peripheral dry-out of the evaporator, several layers of fine copper mesh (mesh number 100) were inserted between the inner wall of the evaporator and a large mesh (mesh number 4), which functions as a plate spring to maintain the gap as illustrated in Fig. 2.

Internal temperature variations of the liquid and vapor and the coolant temperature were monitored using thirty-nine T-type thermocouples installed along the heat pipe as indicated in Fig. 2. Twenty-four thermocouples were installed along the heat pipe, twelve in the liquid and twelve in the vapor region of the evaporator and condenser, every 150 mm to investigate axial temperature variations. In the adiabatic region, four thin-sheath-type thermocouples were installed to measure the vapor temperature and three for the liquid temperature. Six thermocouples

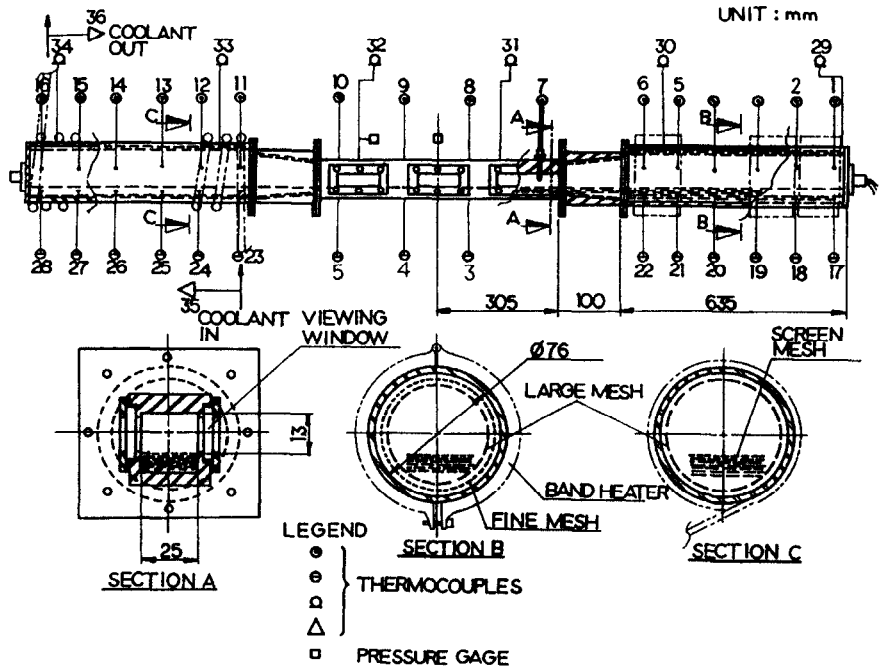

FIG. 2. A detailed configuration and dimensions of the test set-up for heat-pipe experiments.

for monitoring the wall temperatures were installed on the outer top surface every 0.36 m and two thin-sheath type thermocouples for measuring the temperature rise of coolant were inserted in the coolant stream at the inlet and outlet of the coolant jacket. The temperature difference between the inlet and outlet of the coolant was used to estimate the axial heat transport. In addition, two pressure transducers, P. T. #1 and P. T. #2 (pressure range: 0–0.4 MPa (abs)), were installed in the middle and at the end of the adiabatic region, respectively.

Two rotameters (recommended flow rate: 0.063–0.63 l s^{-1} and 0.032–0.32 l s^{-1}), and a water meter (totalizer) were serially connected to the outlet of the coolant circuit to accurately measure the coolant flow rate. At the end of the condenser, a three-way valve was installed to evacuate and charge the heat pipe with working fluid and a micro valve was also attached in order to slowly degas non-condensable gases and control operating conditions when the heat pipe was operating below atmospheric pressure.

Thermal detection of entrainment

Detection of the onset of entrainment was complicated by the fact that various modes of entrainment changed with changes in the flooding height in the adiabatic region. To classify entrainment for the different liquid film thicknesses, a high-speed image analyzer and a high-speed video camera with a shutter speed, 1/4000 s, were used to record the onset of entrainment. These optical techniques, while quite good, encountered problems when the inner wall of the viewing windows were contaminated by the splash from the wavy interface.

Four thermocouples and two pressure transducers were used to continuously measure both the temperature and pressure fluctuations using strip chart recorders at the onset of entrainment. The best locations of the thermocouples and pressure transducers were determined by the experimental observation that the inlet of the adiabatic section may be the most favorable location for entrainment. This results from not only the reduction of the cross-sectional area (higher shear stress in the developing region) in that location but also periodic flooding of the wick (i.e. the wet point tends to oscillate between the inlet and the middle of the adiabatic region) due to the build-up of the hydrostatic head in the condenser. This can be explained by a previous investigation [22], which investigated the pressure distribution in a gravity-assisted heat pipe. Another theoretical idea to support this observation can be drawn from the fact that any interface subjected to a blowing boundary is more susceptible to the formation of interfacial vortices than that under a suction boundary condition. For instance, the inlet of the adiabatic region usually has a cosine velocity profile due to a high radial Reynolds number [25].

If entrainment occurs near the inlet of the adiabatic region, the onset of entrainment was detected thermally by monitoring temperature fluctuations of both liquid and vapor at several representative positions using strip chart recorders. If the conductive heat transport is neglected, the corresponding entrainment limit can be determined by measuring the temperature rise of the coolant and the expression

$$q = \dot{m} c_p \Delta T \tag{44}$$

where $\dot{m}$ and c_p are coolant mass flow rate and specific heat, respectively. In general, the maximum conductive heat transport corresponds to the heat transport sensed by the coolant just before the hot vapor reaches the condenser, and was experimentally measured as about 0.2 kW (4% of 5 kW, which was the typical heat transport at $T_v = 110°C$).

The experimental uncertainty for the measurement of the entrainment limit can be derived from the individual uncertainties in the flow rate and temperature measurements,

- $\delta T_c = 1.0$ K or $\delta T_c/T_c = 0.75\%$—thermocouple uncertainty
- $\delta \dot{m}_c/\dot{m}_c = 0.05$ or 5.0%—specified error limit of the flow meter by the manufacturer

Thus, the uncertainty in the calculation of the entrainment limit is about 5.1 $(=\sqrt{(5^2+0.75^2)})\%$. If the uncertainty due to the contribution of the conductive heat transfer is 4% (i.e. $q_{cond}/q_e \approx 4\%$), the experimental uncertainty for the measurement of the entrainment limit was assumed to be below the maximum uncertainty of 9.1%.

Another significant uncertainty is involved in the measurement of the liquid film thickness, h. In reality, it is very difficult to control h independently from the other operating conditions of a heat pipe. However, the instantaneous, mean liquid depths at the onset of the individual modes of entrainment were found to be nearly constant based upon local configurations of the liquid film recorded by the image analyzer, even though the film thickness was not uniform along the adiabatic region (since higher flooding near the condenser). Typically, uncertainties of the optical measurement might be associated with the flatness of the wick, the rise of the liquid surface contacting the inner side of windows and the optical calibration. Thus, the uncertainty involved in h was estimated to be less than 10% in the sub-millimeter range.

CHARACTERIZATION OF ENTRAINMENT

Before the theoretical criteria are compared with the experimental data, it is necessary to characterize entrainment in both the air–water and steam–water experiments. Three major modes of entrainment were observed. These are (1) wave-induced entrainment, (2) intermediate shear-induced entrainment (or intermediate entrainment) and (3) fully shear-induced entrainment (or shear-induced entrainment). The configurations for each of these are illustrated in Fig. 3 and the three modes are described below.

Wave-induced entrainment

This type of entrainment typically results from roll-waves, which occur when the wick is fully flooded and subjected to increased air/vapor velocity. It was frequently observed in the steam–water experiments when the heat pipe was highly overcharged but rarely in the air–water experiments since the wick was not normally maintained in a fully flooded condition. When the wick is flooded, roll-waves are established at the interface as shown in Fig. 3(a). The stability of this wavy surface may be affected by the interaction of three major forces, surface tension and gravitational forces which tend to stabilize the interface and the viscous drag forces which tend to destabilize it. At the leeward side of the surface, air/vapor pressure tends to be lowest due to the swirling vortices induced by the boundary separation [6–8]. This may cause pressure asymmetry with respect to the wave crest. As a result, liquid bulges are formed and become detached by the air/vapor stream. For the present investigation, the criteria derived from the K–H type instability (equations (12), (19) and (28)) were utilized to predict the onset velocities.

Intermediate entrainment

This type of entrainment is an intermediate stage between the wave-induced and pure shear-induced entrainment. It is the most frequently observed shear-induced entrainment in steam–water experiments and occurs when the capillary-wick is covered with a relatively thin liquid film, whose depth is assumed to be so small that only short waves can propagate in the form of traveling waves as shown in Fig. 3(b). The thin liquid film is bounded by a fixed wicking structure and free surface. Traveling waves (large disturbances) of relatively long wave length are formed due to the hydrodynamic instability of the liquid and grow unstable when the phase velocity is larger than the interfacial liquid velocity [14]. Entrainment is observed as a form of periodical splashes induced by the shearing forces applied to the large disturbances. The viscous K–H instability with finite depth (equation (28)) and the O–S instability by Miles [14] were applied to the critical air/vapor velocity at the onset of entrainment.

Shear-induced entrainment

As the air/vapor velocity continues to increase, the capillary wicking structure is no longer covered with a thin liquid film, thus the liquid menisci are held on the wick as shown in Fig. 3(c). In this case, no disturbance with a wave length larger than the wire spacing is likely to propagate or grow due to the wicking structure, which tends to retard the growth of any disturbance. Hence, entrainment is entirely characterized by the viscous drag force and resisting surface tension force in the individual liquid ligaments held on the wick. This type of entrainment is typically observed in the air–water experiments and not in the steam–water experiments using heat pipes, since it is very hard to obtain the required vapor velocity [5].

RESULTS AND DISCUSSIONS

The critical air/vapor velocity at the onset of unstable waves was determined by the instability cri-

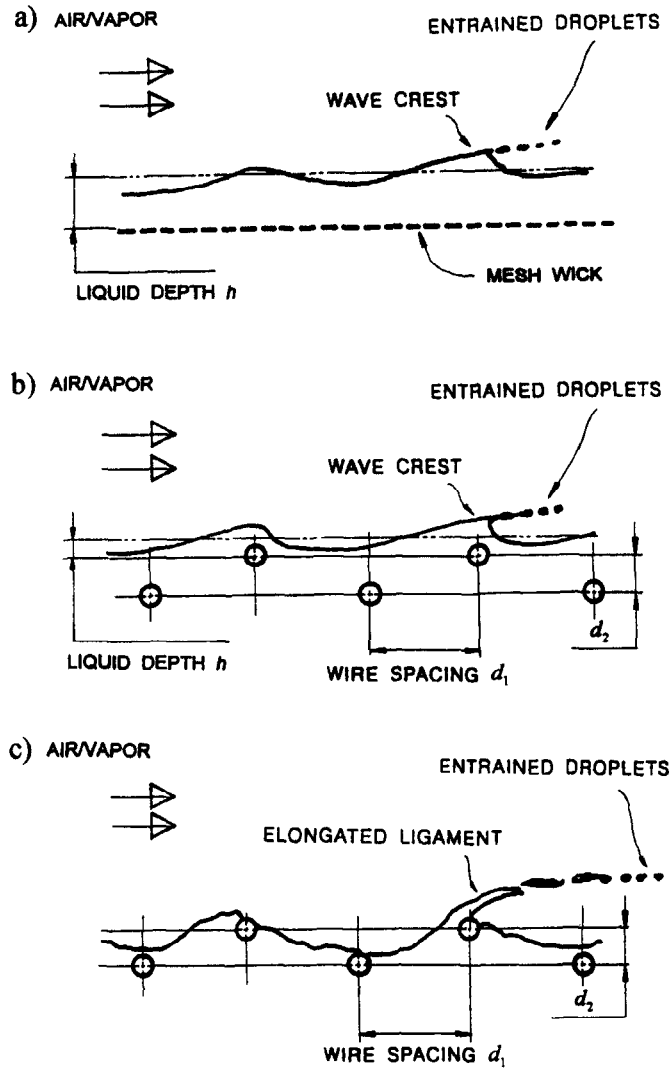

FIG. 3. Various entrainment modes; (a) wave-induced entrainment, (b) intermediate entrainment, (c) shear-induced entrainment.

teria and compared with experimental data corresponding to the onset of various entrainment modes, classified as indicated in Fig. 3. First, the critical air/vapor velocities were calculated from the various instability criteria and the results compared with those from the air–water and the steam–water experiments. Comparisons are presented in terms of liquid film thickness to determine the effect on both the entrainment configuration and the critical velocity. The temperature dependence of the various instability criteria are also investigated using the viscosity number (N_{vi}) and compared with data resulting from the steam–water experiment.

The critical air velocity was obtained using properties of both air and water at 25°C, while the critical vapor velocities for both wave-induced and intermediate entrainment were calculated using property data of the saturated water corresponding to 110°C. In addition, the mesh size employed for both the experimental and theoretical calculations was 40 × 40, resulting in a wire spacing and thickness of 0.58 and 0.28 mm, respectively, as shown in Fig. 3.

Calculation of critical vapor velocities

For the finite depth of the liquid associated with Bondi's model, the critical vapor velocity (saturated water at 110°C) was numerically computed using equations (28) and (29), and presented in Fig. 4 as a function of the wave number, α. The individual curves corresponding to different values of depth show one minimum point and the path connecting the points constitutes the critical vapor velocity defined as the minimum velocity at which unstable waves occur.

For a thin liquid film shown in Fig. 1(b), Miles [14] suggested that $We_{lc} < 3$ was the sufficient stability condition. Thus, the critical liquid Weber number becomes

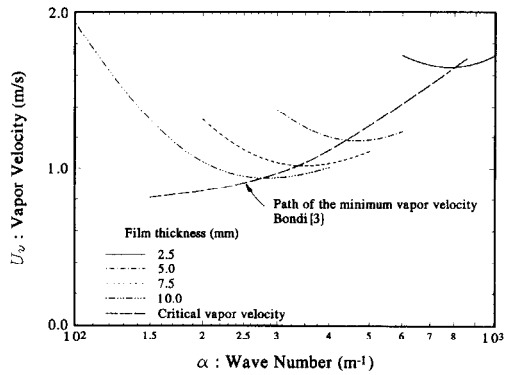

FIG. 4. Critical vapor velocity vs wave number for the finite depth of liquid flow.

$$We_{lc} = \frac{\rho_l U_l h}{\sigma} = 3 \tag{45}$$

where We_{lc} indicates the critical liquid Weber number corresponding to the onset of the instability. For this case, the air/vapor velocity must be determined by equation (45) to obtain the critical vapor Weber number. To do this, the shear stress at the interface was assumed to be continuous and the shear stress on the liquid surface was equated with the frictional shear stress induced by air/vapor flows

$$\tau_i = f_i \frac{\rho_v}{2} U_v^2 = \mu_l \frac{U_l}{h} \tag{46}$$

where f_i is the interfacial Fanning friction factor for wavy annular flows and can be determined by Wallis [24] as

$$f_i = 0.005\left(1 + \frac{300h}{D_h}\right). \tag{47}$$

Here, D_h is the hydraulic diameter of the air/vapor flow. The friction factor, f_i, shows a significant dependency on h for the region, 0.01 mm $< h <$ 10 mm. From equations (45) and (46), U_l can be eliminated and U_{vc} is obtained as

$$U_{vc}^2 = \frac{2\sqrt{3}}{f_i} \frac{\mu_l}{\rho_v h} \sqrt{\left(\frac{\sigma}{\rho_l h}\right)}. \tag{48}$$

By introducing dimensionless parameters, equation (48) can be expressed as

$$We_{vc} = \frac{2\sqrt{3}}{f_i} N_{vi} \tag{49}$$

where We_{vc} and N_{vi} are the critical vapor Weber number and viscosity number, respectively and defined as

$$We_{vc} = \frac{\rho_v U_{vc}^2 h}{\sigma} \quad N_{vi} = \frac{\mu_l}{\sqrt{(\rho_l \sigma h)}}. \tag{50}$$

If both We_{vc} and N_{vi} in equation (49) are expressed in terms of λ_c defined in equation (13) instead of h, then equation (49) can be rewritten as

$$We_{vc} = \sqrt{\left(\frac{6}{\pi}\right)} \frac{1}{f_i} N_{vi} \left(\frac{\lambda_c}{h}\right)^{3/2} \tag{51}$$

where

$$We_{vc} = \frac{\rho_v U_{vc}^2 \lambda_c}{\sigma} \quad N_{vi} = \frac{\mu_l}{\sqrt{(\rho_l \sigma \lambda_c / 2\pi)}}. \tag{52}$$

Comparisons of various instability criteria

In Fig. 5, the critical air/vapor velocities obtained from both the instability criteria and the two experiments are presented as a function of the liquid film thickness. For large h (>0.1 m), the critical velocity predicted by equations (28) and (29) [12] approaches 1 m s^{-1}, which is nearly identical to the experimental results of Jeffreys [7] and Ursell [9], but is significantly smaller than that from the inviscid K–H criterion in equation (12). This is apparently caused by the inappropriate assumptions (no viscous dissipation and long gravity wave for infinite fluids) and implies that the inviscid K–H criterion tends to overestimate the critical velocity corresponding to the onset of unstable waves. As a result, this expression is not valid for use in predicting the lower limit of entrainment onset velocity.

When h has an order of magnitude ranging from 2.5 to 10 mm, the critical vapor velocity calculated from Bondi [12] is approximately 50% lower than the experimental data for the onset of wave-induced entrainment. This large difference implies that the generation of unstable surface waves is not a sufficient condition for entrainment from a finite depth of wavy interface.

The reason for this difference between the two critical velocities may be induced by the sheltering coefficient, C_s, which is suggested to be 0.25 by Bondi [12] (in Jeffreys [7], it ranges from 0.229 to 0.329) and has the same physical significance as the friction factor in wavy liquid film. Clearly, this factor plays an important role in determining the pressure work in the left hand side of equation (26). However, $C_s = 0.25$ has still not been verified for the case of a finite depth since it was originally introduced to obtain the critical air velocity with $h = \infty$ as seen in equation (19).

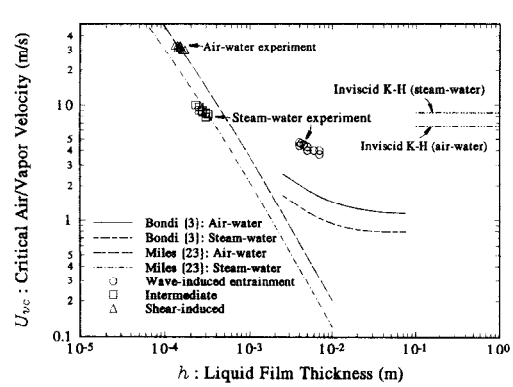

FIG. 5. Critical air/vapor velocity vs liquid film thickness.

Therefore, it may be possible to obtain larger critical velocity than that obtained by Bondi [12] if a smaller sheltering coefficient can be incorporated in equation (26). A 50% decrease in C_s leads to an increase in the critical velocity of approximately 40%.

A second explanation for this difference may be that any growing wave with half of its wave length larger than h (this $\lambda/2$ is referred to as the critical depth) is likely to be decayed [10] even though the pressure work by air/vapor is larger than the energy dissipated as indicated in equation (26). However, as discussed earlier, the depth of liquid (≈ 4 mm) at the onset of wave-induced entrainment is smaller than about 7 mm, that is half of the wave wlength for the given depth (4 mm) according to Bondi's results (given in equations (28) and (29)) [12]. This implies that a portion of the propagating long waves may be decayed so more pressure work (or higher air/vapor velocity) is required to create such an unstable wave that will not decay but grow and eventually result in entrainment.

For the region $1 < h < 10$ mm, extrapolation of Bondi [12] to the point ($h \approx 1$ mm) shows good agreement with the critical velocity calculated from equation (48) which becomes less valid with increases in h since the assumption of a linear liquid velocity profile does not hold. However, the validity of Bondi's prediction for the region ($h \approx 1$ mm) needs to be physically examined in view of Lamb's hypothesis that the possibility of a progressive wave is limited, theoretically, to the case of uniform depth, provided the depth everywhere exceeds half of the wave length [10].

Thus, the physical validity of Bondi's results based on Jeffreys' modification [11] to extend equation (12) to the case of a finite depth should be limited to the region where $h > \lambda/2$ ($h > 2.5$ mm), as shown in Fig. 5. However, the trends of the extrapolated curve could be acceptable since more pressure work (or higher air/vapor velocity) is required to raise such an unstable wave that will not decay but grow and eventually result in entrainment for the region, $h < 2.5$ mm.

For the region with $h < 1$ mm, the critical air/vapor velocity was determined by equation (48) and compared with experimental data, which were classified as intermediate and shear-induced entrainment as shown in Fig. 3(b) and 3(c), respectively. As indicated, the theoretical critical vapor velocity corresponding to the onset of unstable waves approaches the entrainment onset vapor velocity measured in the steam–water experiments. This is a slightly different trend from the case of wave-induced entrainment associated with the fully flooded wick in Fig. 4(a). This implies that once any propagating wave is initiated and starts to grow satisfying the instability condition ($c > 1$), it eventually results in entrainment since increased interfacial shear stress becomes high enough to tear liquid bulges formed by swirling vortices off the leeward side of the broken waves.

The most significant uncertainty in this comparison

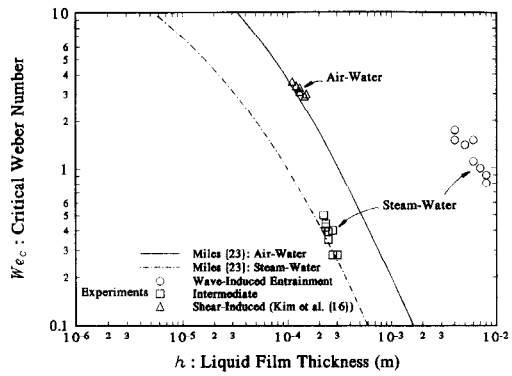

FIG. 6. Critical vapor Weber number vs liquid film thickness.

may be the thickness of the fluctuating liquid film which was optically measured using an image analyzer. Accurate measurement of this thickness may require advanced techniques. For further discussion, detailed dimensions of the mesh (40×40) were examined and compared with the measured film thickness. The results show that the measured film thickness (0.2–0.3 mm) is smaller than the wire spacing (0.58 mm) and is nearly equal to the mesh thickness (0.28 mm). In properly saturated meshes subjected to high velocity vapor flows, this measured film thickness may be a reasonably acceptable dimension.

With further decreases in the liquid film thickness due to the high inertia force of air/vapor flows, the liquid surface recedes from the mesh wick and is held on to the wires as shown in Fig. 3(c). For this case, the theoretical air velocity is compared with the experimental data from the air–water experiments [16] as shown in Fig. 5. The liquid film thickness corresponding to the experimental data is not a measured value but an estimated one based on the theoretical prediction according to equation (48).

The order of magnitude of the estimated film thickness is 0.1 mm, which is smaller than that for the intermediate entrainment and shows an acceptable trend. For the air–water experiment, the validity of equation (48) was not completely recognized since it is very hard to measure the liquid film thickness for this limiting case as shown in Fig. 3(c). However, the correlation between the experimental results and the values predicted by equation (48) is acceptable if the effective film thickness for the case is assumed to be approximately half of the wick thickness (d_2). It should be noted that the validity of equation (48) for this limiting case remains unjustified for the present study.

If h goes to zero, the problem can no longer be solved by equation (48) based on the O–S type instability [14] but can be approximated using spray and atomization theories, since any propagating wave may be decayed by the mesh according to the Lamb's and Busse and Kemme's hypotheses [10, 22].

In Fig. 6, the critical vapor Weber number (We_{vc}) calculated from equation (49) is presented as a func-

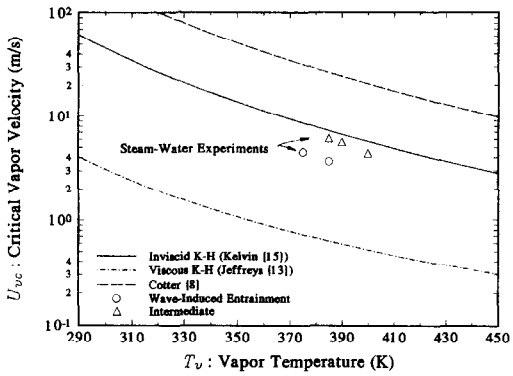

FIG. 7. Critical vapor velocity vs vapor temperature.

tion of liquid depth, h, for the thin film region ($h < 1$ mm). As shown, the trend is nearly the same as that for the critical velocity versus liquid depth indicated in Fig. 5. However, it is even more clear that equation (49) may not be a good indicator of the critical vapor Weber number for the wave-induced entrainment in the region with $h > 1$ mm as discussed earlier.

Temperature dependence of instability criteria

In Fig. 7, general trends for the critical vapor velocities (U_{vc}) predicted by various instability criteria are represented in the variation of vapor temperature and compared with data from steam–water experiments. As shown, Cotter's criterion given in equation (14) shows the highest value of critical vapor velocity and constitutes an upper limit in the prediction. For this limiting case, U_{vc} was calculated by putting $\lambda_c = d_l$ (wire spacing of 40×40 mesh) into equation (14). As noted earlier, this case corresponds to the shear-induced entrainment in Fig. 3(c), hence the trend looks reasonable since this type of entrainment is induced by very high velocity vapor flows, which can usually be seen in air–water experiments but rarely in steam–water experiments using capillary-driven heat pipes.

Similarly, the modified K–H criteria from equation (19) constitute a lower limit in the prediction of the critical velocity. For this calculation, the critical relative vapor velocity (U_r) is assumed to be the same as the critical vapor velocity (U_{vc}) with 0.3 used for the sheltering coefficient, C_s. However, the inviscid K–H significantly overestimate the critical velocity corresponding to the onset of unstable waves in the same manner as indicated in Fig. 5.

In addition, as indicated in Fig. 7, U_{vc} decreases for all the criteria as vapor temperature increases. One reason for the reduction in U_{vc} can be explained by the fact that the vapor densities in the denominators of equations (12) and (14) tend to significantly increase (for instance, ρ_v at 450 K is approximately 250 times larger than that at 295 K), which compensates for the decrease in vapor velocity required to maintain a constant inertia force. Another factor may be due to the decrease in liquid viscosity (e.g. in equation (19)) or viscosity number (Taylor number) defined as N_{vi} in equation (50).

The decrease of vapor velocity at higher temperatures does not imply reduction in the interfacial shear stress (in equation (46)) or pressure work (in equation (26)) since the vapor density tends to significantly increase and compensate for the reduction. Thus, it is hard to determine whether or not a vapor/liquid system will become more unstable and result in earlier instability with temperature increases, even though the liquid is certain to become less stable due to the decrease in the viscosity number N_{vi}.

To accurately determine trends of various instability criteria with temperature change, the critical vapor Weber number (We_{vc}) defined in equation (52) is plotted in Fig. 8 as a function of the corresponding viscosity number (N_{vi} defined in equation (52)) for different ranges of liquid film thickness h.

Similar to the trend shown in Fig. 7, Cotter's criterion is close to the upper limit in the prediction of We_{vc}, while the viscous K–H [7] is near the lower limit. However, We_{vc} versus N_{vi} in Fig. 8 indicates that Cotter [4] and the inviscid K–H [5] are insensitive to variations in the viscosity number, and the modified K–H tends to increase slightly with decreases in the viscosity number. The reason for these trends may be explained by the fact that all these models are less dependent on viscous dissipation than either Bondi [12] or Miles [14].

Results show that We_{vc} from equation (51) tends to decrease as N_{vi} decreases. This implies that the increase in ρ_v/σ in the expression of We_{vc} is not large enough to compensate for the reduction involved in the term, U_{vc}^2. Also, this indicates that h is the most significant parameter in the prediction of We_{vc}. As h decreases, We_{vc} from equation (51) approaches the value determined by Cotter [4] in equation (14), and, for very thin liquid films ($h \approx 0.1$ mm), both show fairly good agreement at lower N_{vi}. At $h = 0.3$ mm, the experimental data corresponding to the intermediate mode of entrainment are accurately predicted by equation (51) and the values of We_{vc} are approximately 10.

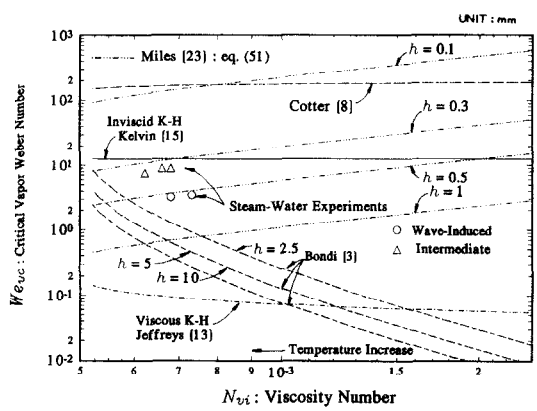

FIG. 8. Critical Weber number vs viscosity number.

For larger h (>2.5 mm), the instability criterion in equation (28) and (29) [12] was employed to determine We_{vc} at the onset of instability. The results in Fig. 8 show that We_{vc} tends to increase significantly as N_{vi} decreases due to temperature increases. This implies that increase in ρ_v/σ in the expression of We_{vc} are large enough to compensate for the reduction involved in the term, U_{vc}^2. It indicates that We_{vc} tends to decrease and approaches the value predicted by the modified K–H criterion as h increases. This is reasonable since Bondi's criterion actually becomes identical to equation (19) as h goes to ∞. However, as shown in Fig. 5, the experimental data corresponding to the wave-induced entrainment are shown to be much greater than predicted by Bondi's instability criterion for liquid depths ranging from 4 to 8 mm.

CONCLUSIONS

Instability theories related to the Kelvin–Helmholtz and the Orr–Sommerfeld problems were reviewed and applied to predict the critical air/vapor velocity at the onset of entrainment from a capillary structure. To compare the theoretical criteria with the experimental results, entrainment observed in both air–water and steam–water situations were characterized and classified into three major categories.

As a result of these comparisons, a modified theoretical criterion based on the results of Miles [14] was developed and used to investigate the effect of liquid depth on the critical air/vapor velocity or corresponding Weber number for the given temperatures. General trends of the various criteria were examined as a function of vapor temperature variation. The important results indicate the following.

(1) Critical air/vapor velocities determined by equation (48) show fairly good agreement with experimental data for the intermediate mode of entrainment in steam–water experiments when the liquid film thickness approaches the wick thickness. For the air–water experiment, the validity of equation (48) was not completely established since it is very hard to measure the liquid film thickness for the limiting case shown in Fig. 3(c). However, experimental results were also well predicted by equation (48) if the effective film thickness for the case was assumed to be approximately half of the wick thickness (d_2).

(2) As h decreases, We_{vc} from equation (51) approaches that determined by Cotter [4] in equation (14), and, for very thin liquid film ($h \approx 0.1$ mm), both show fairly good agreement at lower N_{vi}. At $h = 0.3$ mm, the experimental data corresponding to the intermediate mode of entrainment are accurately predicted by equation (51) and the values of We_{vc} in terms of λ_c are approximately 10.

In the present analysis, only one mesh size (mesh number 40) was examined. However, the effect of mesh sizes on both the film thickness and the resultant critical Weber number may be another topic worth investigating as a future study.

REFERENCES

1. M. Ishii and M. A. Grolmes, Inception criteria for droplet entrainment in two-phase concurrent film flow, *A.I.Ch.E.Jl* **21,** 308–318 (1975).
2. M. N. Ivanovskii, V. P. Sorokin and I. V. Yagodkin, *The Physical Principles of Heat Pipe*, pp. 107–115. Clarendon Press, Oxford (1982).
3. G. P. Peterson and B. Bage, Entrainment limitations in thermosyphons and heat pipes, *ASME J. Energy Resources Technol.* **113,** 147–154 (1991).
4. T. P. Cotter, Heat pipe startup dynamics, *Proceedings of the SAE Thermionic Conversion Specialist Conference*, Palo Alto, California, October, pp. 344–347 (1967).
5. Lord Kelvin (W. Thomson), On the influence of wind, *Phil. Mag.* **42,** 368–377 (1871).
6. M. L. Banner and W. K. Melville, On the separation of air flow over water waves, *J Fluid Mech.* **77,** 825–842 (1976).
7. H. Jeffreys, On the formation of water waves by wind, *Proc. R. Soc. Lond. A* **107,** 189–206 (1925).
8. M. J. Lighthill, Physical interpretation of the mathematical theory of wave generation by wind, *J. Fluid Mech.* **14,** 385–398 (1962).
9. F. Ursell, *Surveys in Mechanics* (Edited by G. K. Batchelor), pp. 216–247. Cambridge University Press, Cambridge (1956).
10. H. Lamb, *Hydrodynamics* (5th Edn, pp. 346–347, 548–549. Cambridge University Press, Cambridge (1924).
11. H. Jeffreys, On the formation of water waves by wind (second paper), *Proc. R. Soc. Lond. A* **110,** 241–247 (1926).
12. H. Bondi, On the generation of waves on shallow water by wind, *Proc. R. Soc. Lond. A* **181,** 67–71 (1942).
13. S. Feldman, On the hydrodynamic stability of two viscous incompressible fluids in parallel uniform shearing motion, *J. Fluid Mech.* **2,** 343–370 (1957).
14. J. W. Miles, The hydrodynamic stability of a thin film of liquid, *J. Fluid Mech.* **8,** 593–610 (1960).
15. V. M. Matveev, Y. N. Filippov, V. I. Dyuzhev and E. V. Okhapkin, Breakaway of a liquid by a gas stream at an interface containing grid, *J. Engng Phys.* **33,** 1008–1012 (1977).
16. B. H. Kim, G. P. Peterson and K. D. Kihm, Analytical and experimental investigation of entrainment in capillary-pumped wicking structures, *Trans. ASME J. Energy Resources Technol.* **115,** 278–286 (1993).
17. P. G. Drazin and W. H. Reid, *Hydrodynamic Stability*, pp. 124–131. Cambridge University Press, Cambridge (1981).
18. E. L. Knuth, The hydrodynamic stability of a thin film of liquid in uniform shearing motion, *Jet Propulsion* **24,** 359 (1954).
19. C. C. Lin, On the stability of two-dimensional parallel flows; part III. Stability in viscous fluid, *Quarterly Appl. Math.* **3,** 277–301 (1945).
20. C. C. Lin, *The Theory of Hydrodynamic Stability*, pp. 39–45. Cambridge University Press, Cambridge (1955).
21. S. W. Chi, *Heat Pipe Theory and Practice*, pp. 33–95. Hemisphere, Washington, DC (1976).
22. C. A. Busse and J. E. Kemme, Dry-out phenomena in gravity-assisted heat pipes with capillary flow, *Int. J. Heat Mass Transfer* **23,** 634–654 (1980).
23. T. B. Benjamin, Shearing flow over wavy boundary, *J. Fluid Mech.* **6,** 161–205 (1959).

24. G. B. Wallis, *One Dimensional Two-Phase Flow*. Wiley, New York (1965).
25. C. A. Busse, Pressure drop in the vapor phase of long heat pipes, *Proceedings of the IEEE Thermionic Conversion Specialist Conference*, Palo Alto, California, October, pp. 391–398. IEEE Press, New York (1967).
26. V. P. Carey, *Liquid–Vapor Phase Change Phenomena*, pp. 90–98. Hemisphere, Washington, DC (1992).